JOURNAL OF QUATERNARY SCIENCE (2018) ISSN 0267-8179. DOI: 10.1002/jqs.3031

JQS Journal of Quaternary Science QRA Quaternary Research Association

Constraining the geometry and volume of the Barents Sea Ice Sheet

SAMUEL B. KACHUCK and LAWRENCE M. CATHLES
Cornell University, Ithaca, NY, USA

Received 21 November 2016; Revised 18 February 2018; Accepted 19 February 2018

ABSTRACT: The ice load configuration of the Barents Sea Ice Sheet (BSIS) over the last glacial cycle is in dispute. The traditional reconstruction, motivated by the observation that paleo-shoreline emergence increases towards the center of the Barents Sea, places a single dome in the center of the Barents Sea at the Last Glacial Maximum (LGM) that collapses to island-centered loads during deglaciation. Observations that suggest that ice flowed from the islands into the Barents even at the LGM motivate another reconstruction that places the ice loads over the islands with minimal marine ice. We analyze an ensemble of ice loads that are consistent with the geophysical observations and show that current relative sea level, GPS and gravity measurements do not and cannot distinguish a central dome from an island-centered BSIS. What is needed are constraints in the central Barents. Improving the gravity data sufficiently will be difficult. However, obtaining even a single GPS uplift rate measurement in the central Barents would resolve the central dome versus island-centered BSIS geometry question. Uncertainty in the Barents Sea ice load geometry provides a good illustration of statistical methods that we believe will be useful in other areas of glaciology. Copyright © 2018 John Wiley & Sons, Ltd.

KEYWORDS: Barents Sea Ice Sheet; GIA; GRACE; optimal experiment design; relative sea level.

Introduction

Marine ice sheets, such as the Western Antarctic, are particularly sensitive to climate change. Insight into the dynamics of such ice sheets is potentially provided by the history of the ice cover of the shallow Barents Sea over the last glacial cycle (Winsborrow *et al.*, 2010). However, the specific configuration of this high Arctic ice sheet during its collapse from the Last Glacial Maximum (LGM) about 20 000 cal a bp (20 ka) to about 10 ka is uncertain (Jessen *et al.*, 2010; Hormes *et al.*, 2013; Hughes *et al.*, 2016). Reconstructions range from a large concentric dome of ice centered in the middle of the Barents Sea (Lambeck, 1996; Grosswald, 2001; Peltier *et al.*, 2015) to a more modest amount of ice concentrated in smaller domes on the surrounding island archipelagos of Svalbard, Franz Josef Land and Novaya Zemlya (Fig. 1; Siegert and Dowdeswell, 1995). Where along this continuum the true ice configuration lies will inform the specific dynamics of its growth and collapse and its application in the fate of similar shallow marine ice-sheets.

An excellent review of the repeated glaciation of the area is given by Ingólfsson and Landvik (2013). There is no question there was grounded ice in the central Barents Sea during the last glaciation (Solheim *et al.*, 1990; Elverhøi *et al.*, 1993). Evidence for this comes from submarine landforms of glacial origin such as mega-scale lineations, drumlin fields and moraines, some of which are indicated in Fig. 1 (Solheim *et al.*, 1990; Hogan *et al.*, 2010). Glacimarine and glacial sediments in the Barents Sea indicate ice grounding (Solheim *et al.*, 1990; Rüther *et al.*, 2011).

Ice divides and domes can be reconstructed using the orientation of sub-glacial features in the seafloor, which indicate ice flow direction. The large marine fan near Bjørnøya (Fig. 1) may indicate flow from the center of the Barents Sea (Winsborrow *et al.*, 2010), but landforms further upstream indicate that a primary ice dome in southern Hinlopenstretet (Fig. 1) between eastern Spitsbergen and Nordaustlandet (Dowdeswell *et al.*, 2010; Andreassen *et al.*, 2014) could also have fed the fan. Andreassen *et al.* (2014) identify such a dome over Svalbard. They raise the possibility that radial ice flow during deglaciation could have overprinted the bedforms indicating flow from an earlier central Barents dome, but do not conclude that this was necessarily so. Dating and lithological studies of glacially transported boulders suggest that even at the LGM there were active local ice domes in north-west Spitsbergen and Nordaustlandet (Hormes *et al.*, 2011; Gjermundsen *et al.*, 2013; Bjarnadóttir *et al.*, 2014). Moraine ridges in the central Barents Sea suggest a dome there (Pavlidis *et al.*, 1990). However, moraines are observed only on its eastern side (Amantov and Fjeldskaar, 2013), which suggests it might have been an extension of the Novaya Zemlya dome's southern margin. High-frequency seismic data suggest the Novaya Zemlya and Franz Josef Land ice sheets were connected across the deepest part of the Sedov Trough at 18 ka (Pavlidis *et al.*, 2001).

One of the main reasons for thinking that the Barents Sea Ice Sheet (BSIS) consisted of a single dome comes from modeling the pattern of glacial isostatic adjustment (GIA) shoreline emergence (a.k.a. relative sea level, RSL) on the surrounding archipelagos (Forman *et al.*, 2004). The emergence on the islands increases towards the center of the Barents Sea (Forman *et al.*, 2004), and extrapolation of the emergence into marine areas suggests a large concentric central Barents ice dome. Previous attempts to fit the emergence data without a large central dome failed to reproduce the observations (Lambeck, 1995; 1996), but only ice models with an ice-free center were considered; models with ice just thick enough to be grounded were not examined. Lambeck (1996) settled on a model which had a single 3.4-km dome south-east of Kongsøya, consistent with other interpretations of the emergence data (e.g. Peltier, 2004).

Terrestrial GPS measurements of the rate of uplift around the Barents Sea have been examined to distinguish between ice models (Auriac *et al.*, 2016). However, like the RSL data, these GPS data are restricted to the peripheral, terrestrial areas. Root *et al.* (2015) analyzed data from GRACE to extract the gravity signal from and infer the timing of the collapse of the BSIS. After applying corrections and filters to reduce the

*Correspondence: Samuel B. Kachuck, as above.
E-mail: sbk83@cornell.edu

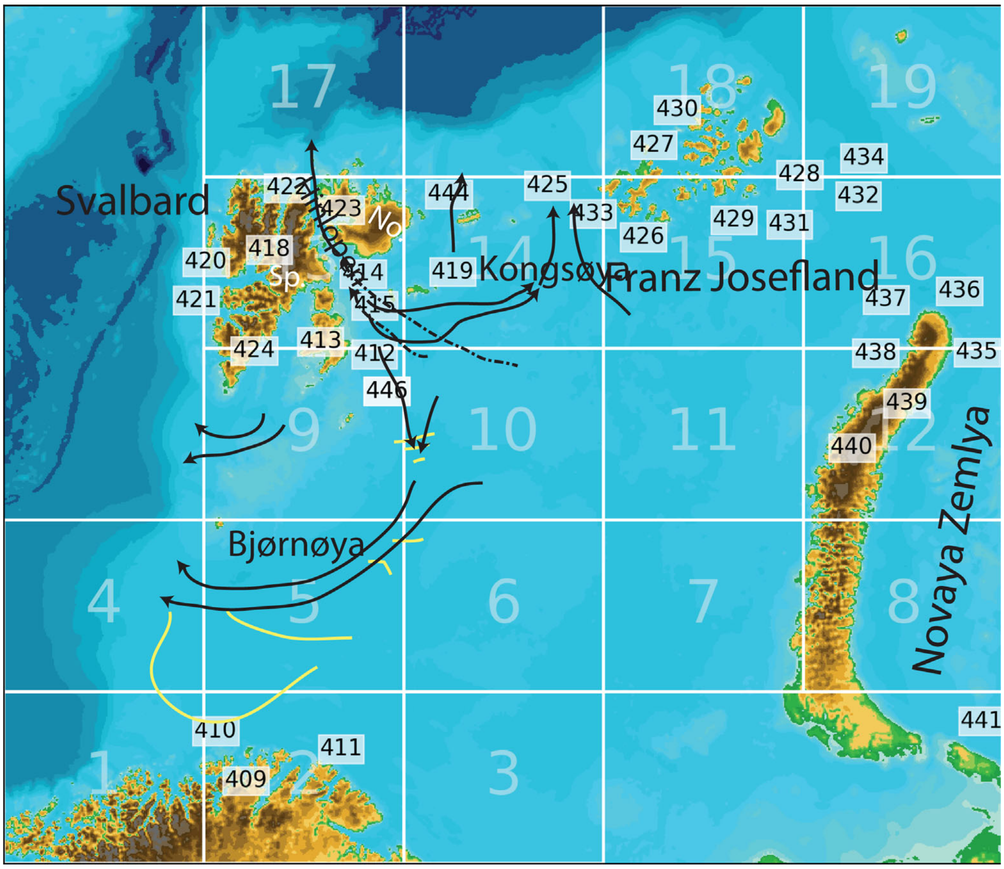

Figure 1. (Color online) Barents Sea ice load areas indicated by white grid with numbers 1 to 19. Small numbers indicate the locations where post-glacial shoreline emergence has been determined (see Table S1 for references). The background color shows water depth from the IBCAO (Jakobsson *et al.*, 2012). Yellow lines indicate moraine positions and black arrows ice flow directions inferred from subglacial features (Ottesen *et al.*, 2007; Dowdeswell *et al.*, 2010; Andreassen *et al.*, 2014; Bjarnadóttir *et al.*, 2014). Dash-dot arrows show flows in the opposite direction, entering Hinlopenstretet (Hinlopen) from the south (Landvik *et al.*, 1998).

influence of present-day ice losses and other sources of error, they infer a central Barents Sea rate of gravity change consistent with the removal of a single marine dome.

The problem of reconstructing the ice in the BSIS from observations of glacial isostatic adjustment on the periphery illustrates the challenges of inverting a sloppy model (Waterfall *et al.*, 2006; Mannakee *et al.*, 2016). This geometric formulation leads to useful insights on the familiar issue that a model's predictive power is not assured by its fit to the data. The Barents presents the same challenge as Antarctica, for example, where the data are on the margins and do not constrain model behavior in the interior (e.g. Nield *et al.*, 2014). The essential character of a sloppy model is that it is controlled only by a small subset of well-constrained 'stiff' parameter combinations. The other, 'sloppy', parameter combinations are free to vary over a large range without affecting the fit, but do not constitute an obvious null space. For the BSIS, the ice in the marine areas is sloppily constrained even when, as shown here, both the RSL and the gravity constraints are imposed.

The purpose of this paper is to determine how well RSL and GRACE data constrain the ice load geometry, and to identify where new data would be most useful. After introducing the methods of analysis and the theory of sloppiness, we perform an inversion for deglaciation curves in the Barents Sea and show that it provides insights and information that are not obvious and not easily otherwise attained.

Modeling and estimation methods

GIA modeling

To model the response of the Earth's surface to glacial loads, we use a gravitationally self-consistent approach to solving the global sea-level equation that accounts for the viscoelastic and gravity response of a loaded spherically symmetrical, non-rotating Earth following the quasi-spectral method of Cathles (1975) (Kachuck, 2017). The equations of motion for elastic and viscous displacements and gravitational perturbations in response to a spherical harmonic load are added together at each time step to obtain the viscoelastic deformation and gravity perturbations at the solid surface. The response curves for each order number are convolved with the spherical harmonic decomposition of the changing ice load in the time domain. Performing the calculation in this way allows us to constrain water load changes consistent with coastline topography without iteration (Kendall *et al.*, 2005). The calculations are performed to order number 288, which corresponds to a spatial resolution of 35 km in the Barents Sea. Although the calculations presented focus on the Barents Sea, they treat the ice and sea-level redistribution over the entire globe, which is assumed to be in a state of isostatic equilibrium at the end of the last interglacial.

For radial elastic parameters and density we use PREM (Dziewonski and Anderson, 1981). For viscosity, we use the preferred rheological profile of Fjeldskaar (1994) for Fennoscandia and the Barents Sea: a uniform mantle at 10^{21} Pa s overlain by a 75-km $10^{19.6}$ Pa.s asthenosphere and a lithosphere with an effective elastic thickness of 30 km.

The global ice load is defined every thousand years since the LGM ($\sim$ 20 ka to present) based on the ice margin positions, assumed lithology-dependent basal shear strength and environmental conditions (Amantov and Fjeldskaar, 2017). The ice model honors the global meltwater curve of Bard *et al.* (1990). The loading cycle (growth phase) starts at 120 ka and is constructed assuming that times with identical eustatic sea level have identical ice loads. There is no change in ice mass from 4.5 ka to the present, but the continued isostatic response of the ocean basin has a large effect on the present-day calculated gravity and uplift rates. Therefore, the

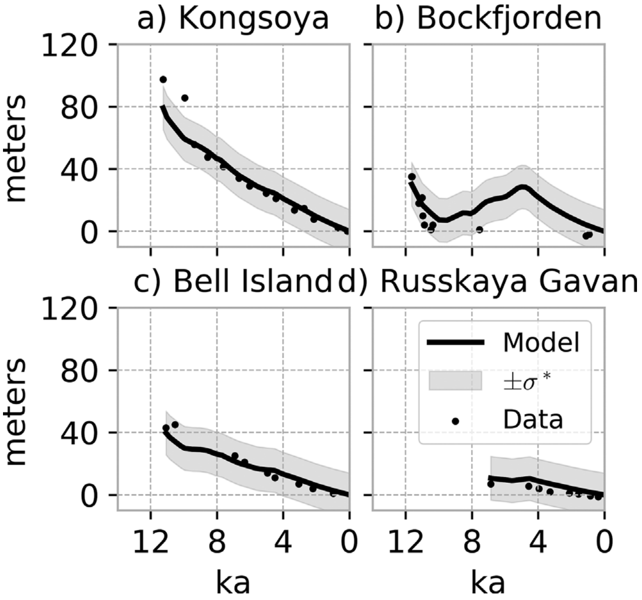

Figure 2. Examples of best-fit relative sea-level (RSL) predictions (solid lines) with their 1-sigma error range (shaded) of RSL change are compared to RSL measurement (solid dots) at four sites. Plots for every location are given in Fig. S2.

recent water load redistribution is computed every 125 years. Time slices of the BSIS can be found in the Supporting Information,Fig. S1.

An obvious question is whether the mantle rheology and the initial ice load history would make a difference to the conclusions reached in the analysis. We address this question by performing the same analysis with the VM2 rheology and its preferred global ice load ICE-5G (Peltier, 2004). The effects of these very different earth and ice models on the inversion results are minimal. Neither the volumes estimated nor the configurational uncertainty are significantly changed (Appendix S3).

Ice volume estimation methods

The ice load in the BSIS is divided into 19 equal area sections (Fig. 1) whose deglaciation volumes can be altered independently with a single scaling factor k_i (see Fig. 3 below), which modifies the average ice load in the area at the LGM. The shape of the ice in each area is unchanged from the initial deglaciation history, but ice loads at all times in area *i* are multiplied by the dimensionless parameter k_i. This is similar to the ice modification method used by Simon *et al.* (2016). Our approach uses much smaller areas whose volumes we modify simultaneously, rather than sequentially.

The grid of areas covering the Barents Sea was chosen so that: (i) the archipelagos would be covered by separate areas; (ii) the areas covering Svalbard (area 13) and Franz Josef Land (15 and 18) would have a full area between them (14); and (iii) most areas would have ice for several stages before being deglaciated (4 and 17 are exceptions). Only a small amount of the BSIS is not contained in the 19 sections. Less than 5% of the BSIS ice volume at the LGM is excluded and it lies in parts of the north and south-east of the Barents Sea that are quickly deglaciated when the ice first starts to retreat. The result is that a 19-dimensional vector *k* defines the modification of the BSIS.

We use a probabilistic framework to infer the scaling factors *k* from observations of glacial isostasy. From a uniform prior, the posterior probability for the parameters *k* given a vector of *n* observations *d* and a model that predicts those observations $\mathbf{g}(\mathbf{k}; E, I)$ with errors σ is written as:

$$P(\mathbf{k}|\mathbf{d}) = \frac{1}{(2\pi\sigma)^{n/2}} \exp\left(-\frac{1}{2}\left(\frac{\mathbf{d}-\mathbf{g}(\mathbf{k})}{\sigma}\right)^2\right). \quad (1)$$

In Eqn 1, the model $\mathbf{g}(\mathbf{k})$ depends on the choice of a viscosity profile *E* and unmodified ice load history *I*, which necessarily trade off with one another. While we do not include this trade off in the analysis, we show in *Appendix* S3 that an analysis which uses a very different viscosity profile and starts with a very different ice load history produces an almost identical result. The probability distribution in Eqn 1 is sampled using a Markov chain Monte Carlo method (Foreman-Mackey *et al.*, 2013) to derive an ensemble of BSIS ice configurations that are compatible with the observations. The mode of this sampled distribution is chosen as the best-fit configuration.

Implicit in Eqn 1 is the assumption that the expected errors between the observations *d* and the modeled values of these observations *g* are independently drawn from a single normal distribution. Errors in measuring RSL involve errors in the heights of shoreline samples and calibration uncertainties in carbon-14 dating, which can be combined into a combined height error or treated separately (Mitrovica *et al.*, 2000). We assume that the RSL height errors of all measurements are distributed with the same normal distribution of width σ_{RSL}, and include σ_{RSL} as a parameter to be estimated by maximum probability (Appendix S1; Fig. S4). We therefore have a parameter set $\theta = \{k, \sigma_{RSL}\}$ whose posterior distribution $P(\theta|\mathbf{d})$ will be sampled.

Covariances of the parameters can be computed directly from *N* samples of θ from the posterior distribution or approximated:

$$C_{ij} = \frac{1}{N}\sum_{\alpha=1}^{N}\left(\theta_{i,\alpha}-\bar{\theta}_i\right)\left(\theta_{j,\alpha}-\bar{\theta}_j\right) \approx \frac{1}{2}\left[J^T J\right]_{ij}^{-1} \quad (2)$$

where $\bar{\theta}_i$ is the mean of parameter θ_i and *J* is the Jacobian of the residuals at the optimal point θ^* with components

$$J_{ij} = \frac{\partial}{\partial\theta_j}\frac{g_i(\mathbf{k})}{\sigma}\Big|_{\theta*}. \quad (3)$$

In the above, $\theta^* = \{\mathbf{k}^*, \sigma^*\}$ are the best-fit parameters determined during sampling as the mode of the sampled posterior distribution.

A universal feature of non-linear models is a hierarchy of parameter sensitivities, with strong dependence on the values of a few well-constrained, ‘stiff’ combinations of parameters and increasingly weaker dependence on all other ‘sloppy’ parameter combinations (Waterfall *et al.*, 2006). Sensitivities spanning many orders of magnitude can be looked at as global geometric characteristics of the mapping from parameters to observations that can be investigated locally through the $J^T J$ sensitivity matrix. The $J^T J$ matrix is characterized by eigenvalues that evenly span many orders of magnitude, reflecting the hierarchy of constraints. The eigenvectors of $J^T J$ are the linear combinations of parameters that are independently constrained. Because there are commonly large tradeoffs between parameters, each eigenvector typically depends on many parameters.

Recognition of a model’s sloppiness provides an important perspective on the model’s predictive usefulness. Because the model is unresponsive to the sloppy parameter combinations,

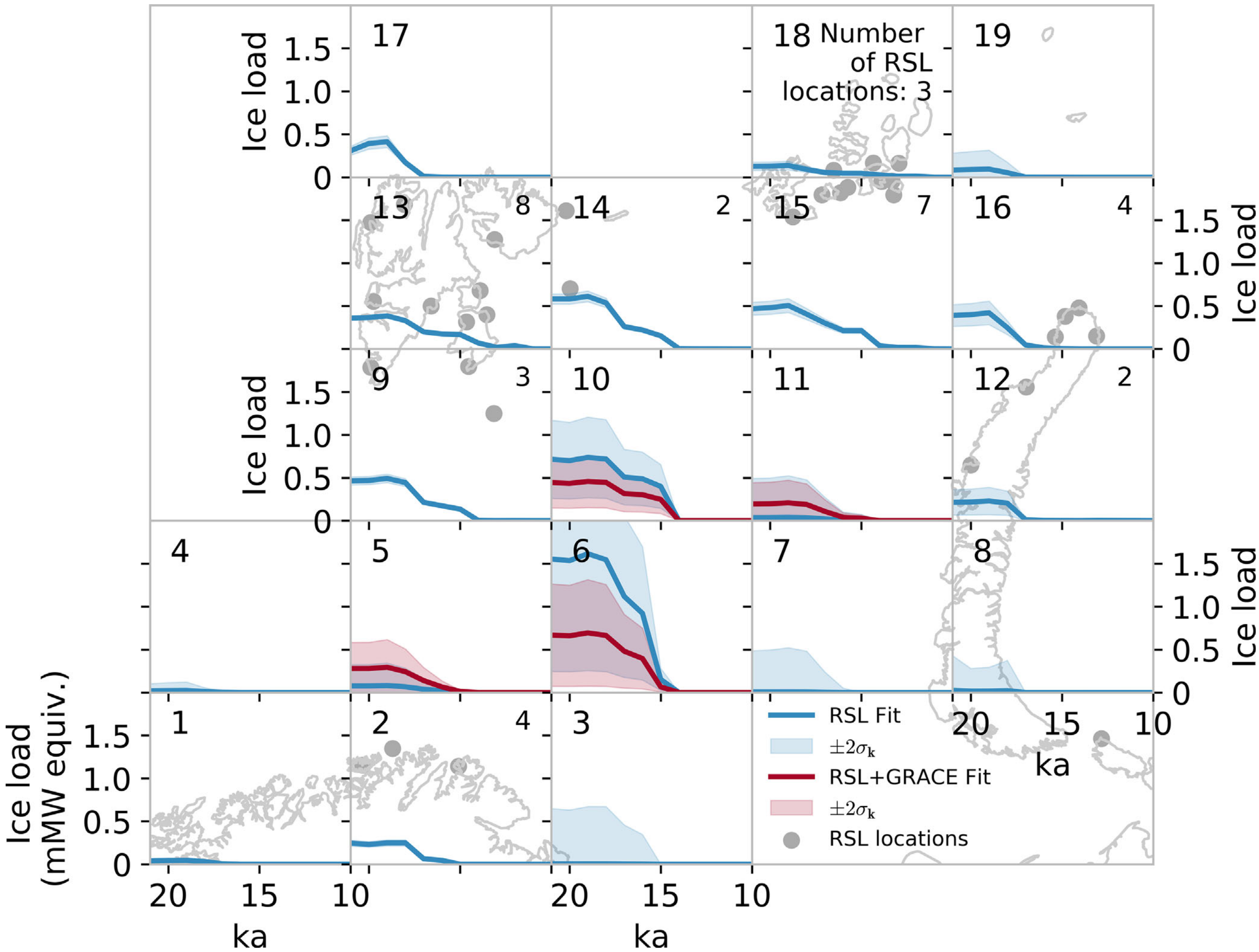

Figure 3. (Color online) Best-fitting average ice load histories in each of the 19 areas. The best-fit ice volume (in meters meltwater equivalent; mMW equiv.) and 2σ uncertainty range if the ice is constrained with RSL measurements alone (blue) or in addition to GRACE gravity data (red, for areas that are significantly affected). Substantial ice in the northern Barents Sea (area 14) is indicated. The GRACE data reduce the uncertainty in the central Barents Sea ice load but does not rule out a substantial marine dome or just-grounded central ice sheet. The dots show data locations from Table S1.

many predictions from the model can be quite accurate even while the sloppy parameter combinations are unconstrained. A consequence is that to constrain a parameter to within, say, 10% by taking new data from the same locations can require an unrealistic quantity and quality of data (Apgar *et al.*, 2010; Chachra *et al.*, 2011).

We will focus on a particular prediction as a proxy for ice configuration: the LGM total ice load volume of the BSIS, V_{LGM}. The uncertainties in the ice-modifying parameters propagate linearly to this prediction as

$$\mathrm{Var}(V_{\mathrm{LGM}}) \approx \frac{\partial V_{\mathrm{LGM}}}{\partial \mathbf{k}} \left[2J^T J\right]^{-1} \frac{\partial V_{\mathrm{LGM}}}{\partial \mathbf{k}}. \tag{4}$$

(see Casey *et al.*, 2007). To compute the expected reduction in variance of an additional observation d' that can be measured to an accuracy $\sigma_{d'}$, we add the new observation to data d and model prediction g, and re-optimize. A shortcut to assess the reduction is to update the Jacobian approximation of the errors. The new data prediction g' adds a row to the model Jacobian given in Eqn 3, which results in the rank-1 update to J^TJ:

$$J^T J \rightarrow J^T J + \frac{1}{\sigma_{d'}^2} \frac{\partial g'}{\partial \theta}\bigg|_{\theta^*} \frac{\partial g'}{\partial \theta}\bigg|_{*\theta^*}^{T}, \tag{5}$$

where θ^* is the optimal parameter vector before including the new candidate point. *Appendix* S2 gives a detailed explanation. The updated Jacobian in Eqn 5 can be used to compute the new variance of the prediction V_{LGM} for possible d', and to select the one that maximizes the reduction in variance, a process called optimal experiment design (Casey *et al.*, 2007; Mannakee *et al.*, 2016).

Data

The main constraints on ice volume are the RSL records on the archipelagos surrounding the Barents Sea and northern Scandinavia (see Table S1 for all locations and citations). Distributed among 34 locations, there are in total $n = 368$ emergence observations. The calculated (GIA model) RSL is interpolated from the calculation grid to the locations and ages of the observed data.

The GRACE data considered here are digitized from the processed results of Root *et al.* (2015), Fig. 2, who report the maximum gravity rate in the central Barents Sea. Their rate is extracted after removing the recent melting of ice on Svalbard and smoothing to isolate the gravity signal of glacial isostatic rebound from the long-wavelength gravity signal of Greenland and short-wavelength sources of noise. They use a Gaussian bandpass with a highpass wavelength of 600 km and lowpass wavelengths varying from 210 to 300 km in 10-km increments. Notably, as the processing method cannot identify the location of the maximum gravity rate, important information about ongoing GIA is lost.

Our consideration of GPS deformation observations in the Barents Sea is restricted to the vertical uplift at the sites reported by Auriac *et al.* (2016), which are also corrected for present-day melt in Svalbard.

Results

The fit

Figure 2 compares RSL measurements (dots) to the GIA model predictions (lines with $\sigma^*_{\mathrm{RSL}} = 14\,\mathrm{m}$ uncertainty bands) for the best-fitting set of ice modifications $\mathbf{k}^*$. The best-fit ice model is the mode (highest probability) of 800 $\mathbf{k}$ vectors sampled from the posterior distribution (Eqn 1). This ice configuration reproduces many of the features of GIA. Analysis of the residuals (Appendix S1) indicates that the best-fit error model of $\sigma^*_{\mathrm{RSL}} = 14 \pm 0.7\,\mathrm{m}$ appropriately accounts for systematic uncertainties in the model of RSL. This estimate includes the tens of meters of observational error (Mitrovica *et al.*, 2000) in the RSL measurements as well as sources of systematic error. For instance, our model does not include changes in the Earth's rotation, whose omission represents an insignificant error of approximately 1 m (Milne and Mitrovica, 1998).

The spread of V_{LGM} (the volume of the BSIS at the LGM) around the best-fit parameters, calculated by applying Eqn 4 to the sampled parameters, is centered at $5.61 \pm 0.59\,\mathrm{m}$ meltwater equivalent (mMW equivalent). This 10% uncertainty seems small, but encompasses a wide range of possible configurations in the central Barents Sea.

This surprising range is illustrated in Fig. 3. The best-fitting deglaciation curve with its region of uncertainty (shaded band) is plotted in each ice load modification area. The blue lines and shading show the fit conditioned on the RSL observations. The red line and shading show the fit conditioned on both the RSL and the GRACE gravity data. The impact of the GRACE data on the uncertainty is limited to only a few areas, so only these areas are shown. The figure illustrates the large variations in uncertainty from area to area, and predicts a substantial ice load in the northern Barents Sea (area 14) between Svalbard and Franz Josefland, confirming at least a northern marine dome. The central Barents Sea (areas 6 and 10) carries the most uncertainty, and the ice load there ranges from a large ice dome to nearly no ice loading (just-grounded ice), illustrating that the GRACE gravity data do not settle the question of whether there was a domal ice sheet in the central Barents Sea at the LGM.

Sloppiness in the Central Barents Sea

Figure 4 shows the eigensystem of the J^TJ matrix at the best-fit point. Figure 4(a) illustrates the broad spread of the 19 eigenvalues. Figure 4(b) illustrates the eigenvector matrix. Each column in the eigenvector matrix is the projection of an eigenvector on the 19 ice-modifying scaling factors k, with each cell's shading showing how much that area contributes to the eigenvector and the color indicating whether the contribution is positive (red) or negative (blue, hatched). Because the eigenvectors are invariant to reversal of sign, what matters is the sign relative to the other areas in the eigenvector. The eigenvectors are arranged in order of increasing uncertainty (decreasing eigenvalue) along the x-axis of Fig. 4(b). The ice model areas are arranged (bottom to top) by the number of RSL observation locations they contain. Below the solid black line, the ice areas have no RSL observations and are arranged in order of their decreasing eigenvalues so the matrix is approximately diagonal.

The eigenvalues are sloppy: their magnitudes are spread evenly across almost five orders of magnitude, with some eigenvectors even smaller. The eigenvalues are normalized by the largest eigenvalue to make this spread easier to observe. The eigenvectors with these smallest eigenvalues are associated with areas 3, 4, 7 and 8, all of which are determined by the inversion to have had just-grounded ice (i.e. almost no net load) as the most likely scenario given the RSL data. The RSL data require no ice load here and the only constraint is that there was just-grounded ice. These very small eigenvalues cause the total LGM ice volume standard deviation (the square root of Eqn 4) to be far larger than what is sampled (5.61 ± 53.73 mMW equivalent). However, when these four eigenvectors are omitted by zeroing them in a singular value decomposition of J, the approximated LGM ice volume standard deviation from Eqn 5 is reduced to 5.61 ± 0.60 mMW equivalent, which is almost identical to the 5.61 ± 0.59 mMW equivalent uncertainty computed from the sampled parameters. This process does not entirely remove the uncertainty of the volumes in these areas, however, because these areas contribute non-trivially to other eigenvectors.

The ice modification areas associated with the stiffer directions are those which contain the most RSL data, and hence the concentration of dark squares at the top left. Similarly, the areas associated with the sloppiest directions are in the central Barents Sea. Ice can be taken out of the central Barents Sea, added to it or shifted between areas within it, with little to no effect on the model RSL predictions on the archipelagos.

Optimal experiment design

Can we predict which data might better constrain the ice volumes in the central Barents Sea? We consider two additional sources of data: gravity rates derived from GRACE and uplift rates measured by GPS stations. We include the gravity in the fit by appending the GRACE-derived gravity rates in fig. 2a of Root *et al.* (2015) to our data vector d and amending our GIA model g. The errors for these measurements, σ_{GRACE}, are taken as the 1σ bars from the same published figure that reflect the uncertainty in how modern melt from Svalbard affects the gravity signal.

As before, these data are fit using Markov chain Monte Carlo sampling. The best-fitting ice volumes and their uncertainty bands are shown in red in Fig. 3 for the few areas where the ice volumes are changed enough by including the gravity data to warrant display.

Equation 5 (via Eqn S2) predicts that the expected reduction in the standard deviation for V_{LGM} from including one of the filtered observations is 0.11 mMW equivalent. The total ice volume uncertainty is reduced from 5.61 ± 0.62 to 5.61 ± 0.51 mMW equivalent. After refitting the parameters, the new actual LGM volume and uncertainty is 5.01 ± 0.36 mMW equivalent, indicating a realized uncertainty reduction of 0.26 mMW equivalent. However, the crucial problem of discriminating between a significant and minimal Barents Sea ice load is left unresolved by the GRACE results because along with the reduction in uncertainty there is a reduction in the most likely maximum load in areas 6 and 10 and a slight increase in areas 5 and 11, so that neither end case (minimal or maximal central Barents Sea ice load) is sufficiently excluded.

To better appreciate the breadth of possible configurations that are equally likely given the RSL and GRACE data, Fig. 5 shows the results from a sample ice load one standard deviation above the mean ice load volume ($+1\sigma$, 5.37 mMW

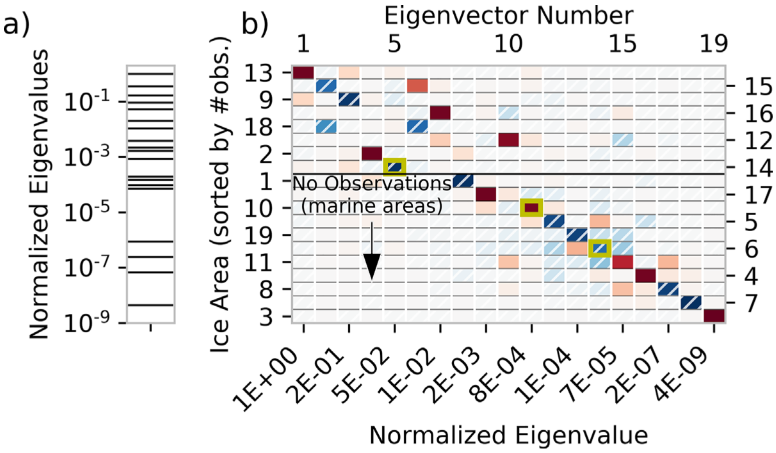

Figure 4. (Color online) Eigensystem for $J^T J$ at the point of best fit between calculated and observed RSL. (a) The eigenvalues, normalized to their largest value, are spread evenly over a wide range. (b) The eigenvector matrix. The eigenvectors (columns) are arranged from left to right in order of decreasing eigenvalue. Shading represents how much each ice modification area contributes to each eigenvector (blue/hatched is negative). The rows (areas) are arranged in decreasing order of the number of RSL data sites (see text).

equivalent) and one standard deviation below (-1σ, 4.65 mMW equivalent). These ice models are primarily distinguished by the amount of ice in the central Barents Sea (areas 6, 7, 10 and 11 have an LGM volume of 1.53 versus 1.19 mMW equivalent; see Fig. 5a,b).

Figure 5(c,d) compare the different present-day rates of gravity change. As expected, the maximum change rate (signified by the white 'x') is further south and larger (0.52 μGal a^{-1} versus 0.47 μGal a^{-1}) in the large ice load ($+1\sigma$). The rates of gravity change surrounding the central Barents Sea are unaffected. After filtering with a bandpass filter of 230–600 km (Fig. 5e,f), the difference in the magnitudes decreases by half (0.184 versus 0.161 μGal a^{-1}) and the distance between the maximum rates of gravity change (signified by the white 'x') also diminishes. The GRACE gravity field with this filter yields a maximum rate of 0.163 ± 0.030 μGal a^{-1} (Root *et al.*, 2015). The RSL contours from 10 ka for the larger ($+1\sigma$) and smaller (-1σ) ice loads are almost identical where RSL observations have been made (black dots, Fig. 5g,h). Whereas the contours going through the data locations are approximately equivalent, the shape just away from these locations is markedly different.

The present-day uplift in response to the $+1\sigma$/-1σ loads, shown in Fig. 5(i, j), reveals a large difference in the central Barents Sea. In response to the $+1\sigma$ load, the central Barents Sea uplifts with a maximum rate of 7 mm a^{-1}, whereas that same location subsides at about 3 mm a^{-1} in response to the -1σ load. The location of the existing GPS stations around the Barents Sea (black dots in Fig. 5i, j) records similar uplift rates for the $+1\sigma$ and $-\sigma$ ice loads, and indeed the entire ensemble of possible ice loads is consistent with the RSL and GRACE data.

By contrast, the experimental design formalism identifies a location (the cross in Fig. 5i, j) where a single uplift rate measurement with a moderate uncertainty would resolve the central Barents Sea ice thickness question. Figure 6(a,b) shows the results of applying experimental design to a grid of candidate uplift rate observations, assuming the uplift rate can be measured to within 0.5 mm a^{-1} (as in Auriac *et al.*, 2016–other errors are shown in *Appendix* S4; Fig. S6). Predictions of present-day uplift rate at individual sites within the Barents Sea are mostly sensitive to small changes in the nearest ice load modification area, so it is reasonable that the most discriminating observations would be drawn from the areas with largest uncertainty in ice load. Such measurements are increasingly possible as improvements are made in underwater measurements, such as with combined acoustic and GPS techniques, although uncertainties (~2 cm a^{-1}) are presently too large (Honsho and Kido, 2017).

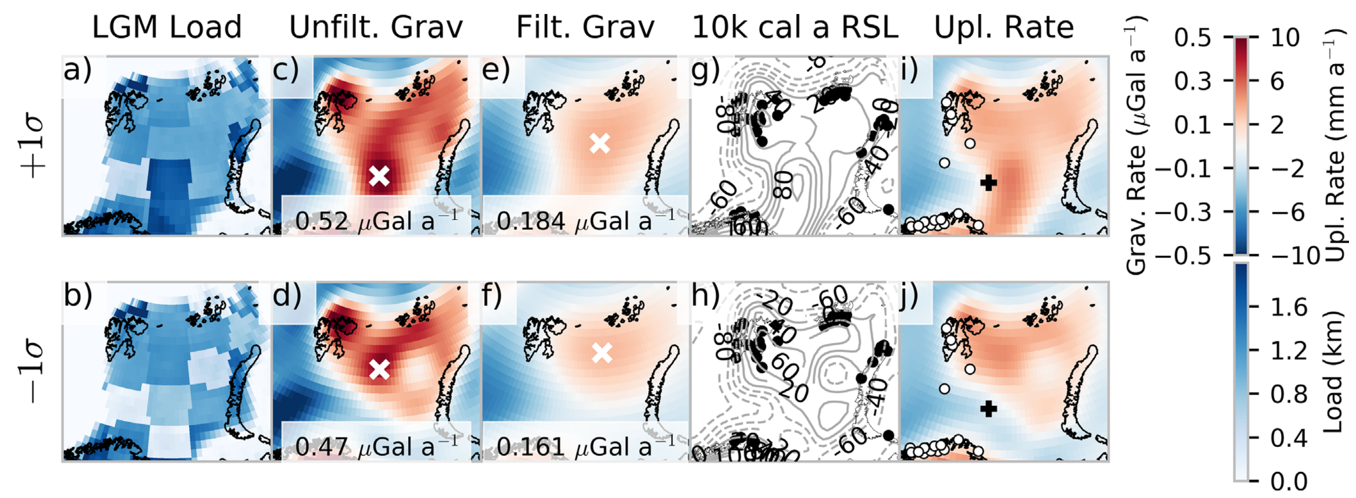

Figure 5. (Color online) Differences between an ice model 1σ above (top row of figures) and 1σ below (bottom row) the RSL + GRACE posterior mean. (a,b) Water-load equivalent of the ice models. Calculated unfiltered (c,d) and filtered (e,f) model rate of gravity change, with the maximum rate of change indicated by an 'x' and the rate of gravity posted in the upper right. The filter is a 230–600 km bandpass filter. (g,h) RSL contours at 10 ka with RSL data locations shown as dots for comparison with fig. 6 of Forman *et al.* (2004). (i,j) Present-day uplift rate, with dots indicating the GPS locations in Auriac *et al.* (2016) and the cross indicating the location of maximum V_LGM variance reduction identified by optimal experiment design (as in Fig. 6).

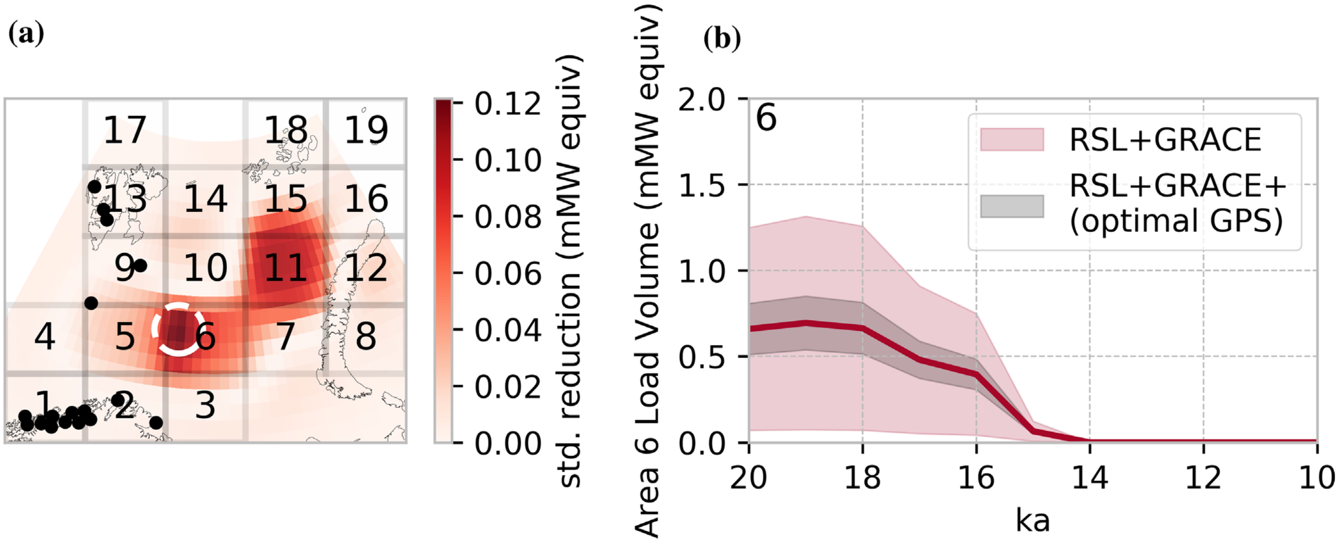

Figure 6. (Color online) (a) Optimal reduction in Barents Sea LGM ice load volume that can be achieved with a single observation of the uplift rate with a 1σ error of 0.5 mm a^{-1} is centred on 73.7°N, 32.5°E, as shown by the dashed circle with a radius of 1° (~70 km). Dots show GPS data locations referred to in Auriac *et al.* (2016); all are far from this area. (b) Reduction in uncertainty in ice load of area 6 with the optimal uplift rate measurement of 1.9 ± 0.5 mm a^{-1} is illustrated by the tightening of the uncertainty band from the red band (also shown in Fig. 3) to the black band. See Fig. S5(c) for the optimal measurement using VM2 and ICE-5G.

The small dots in Fig. 6 show the locations of available GPS data, as reported by Auriac *et al.* (2016). All lie in areas of very low information gain. The nearest extant station is the Bjørnøya site (BJOS) near the corner of areas 4, 5 and 9, which has an expected reduction to the uncertainty of V_{LGM} of just 0.02 mMW. The predicted maximum reduction in the uncertainty of V_{LGM} is just over 0.1 mMW equivalent within a degree of 73.7°N, 32.5°E (indicated by the white dotted circle in Fig. 6a) so Bjørnøya offers an uncertainty reduction that is small compared to the reduction that is possible. Substantial gains might also be had from a measurement in area 11 (which is tied to area 6 as indicated by eigenvectors 13 and 14 in Fig. 4). An uplift rate measurement at the optimal location in area 6 would reduce the ice load uncertainty band as illustrated in Fig. 6(b) for a hypothetical measured GPS uplift rate of 1.9 ± 0.5 mm a^{-1}. A single measurement would distinguish a minimal central Barents Sea ice load from a single contiguous dome.

Discussion

Regional independence

This paper shows that inferring the configuration of the BSIS from the current observations of glacial isostatic adjustment exhibits sloppiness. The ice volumes of areas with high data density (areas 13, 15, 18 and 9 in Fig. 3) and the areas proximal to the data-rich areas (14) must have had substantial ice at the LGM, and ice volumes in the marine areas (e.g. 5, 6 and 7) are unconstrained by observations. Starting with the 11th eigenvector in Fig. 4(b), which coincides with area 10 in the center of the Barents Sea, the sloppy parameters are mostly associated with marine areas in the southern Barents Sea or areas in the periphery (such as 8, 17 and 19) that were never covered with much ice. Each of these eigenvectors is dominated by a single area.

Typically sloppiness is associated with complicated trade-offs between parameters (Mannakee *et al.*, 2016). Thus, it is surprising that the order of the ice areas in the eigenvector matrix of J^TJ can be arranged so sections of the matrix are so close to diagonal. We expected tradeoffs, for example, between ice volumes in the Barents Sea because of the smoothing effects of the lithosphere (Cathles, 1975). The diagonality of the J^TJ eigenvectors indicates that GIA around the Barents Sea is largely controlled by the local ice load, and suggests that a better fit would require more local tailoring. Figure S5 in *Appendix* S3 shows that the diagonality remains even if the lithosphere is very thick. The ability of the eigenfunctions to reflect local ice interdependencies is illustrated very briefly in *Appendix* S1.

A related concern might be that we have introduced artificial independence by allowing steep slopes along the boundaries of the modification areas. This independence could be broken by introducing a prior constraint on the ice modifying parameters (e.g. Stokes *et al.*, 2015). However, these steep slopes have no effect on the viscoelastic rebound. Short-scale features, like these slopes, are elastically supported by the lithosphere, so the load as seen by the mantle is much smoother, as exemplified in Fig. S3. Imposing prior constraints on ice sheet smoothness could prejudice the inversion and would prove inappropriate in light of the conflicting interpretations of bathymetric observations noted in the Introduction.

Consideration of the sloppiness in the estimated ice parameters has afforded us a formal view into the dependencies between ice load, Earth rheology and observations of glacial isostasy. It shows that constraints on the volume of the BSIS cannot come from further RSL data points on the archipelagos, continued terrestrial GPS monitoring or the current GRACE measurement. A new method of processing the GRACE signal or a measurement of uplift rate from the marine region is required. The analysis provides insights that could not be otherwise easily obtained and are important. For instance, it is surprising but significant that reducing the error on the inferred GRACE gravity change rate to zero would provide negligible additional constraint on total ice volume and its configuration.

Conclusions

The purpose of this investigation was to determine how well the configuration of the BSIS at the LGM can be constrained by observations of GIA from existing measurements of relative sea levels, rates of change of gravity and GPS surface uplift rates. We have presented a geometric perspective on sensitivity analysis that highlights how the five order-of-magnitude range of sensitivity to parameter combinations results in regionally well-constrained ice loads on the archipelagos but very poorly constrained ice loads in the marine areas of the Barents Sea. Many of the specific features of GIA depend on the local ice load, so that a large range of regional ice loads fits the record of paleo-shoreline emergence record.

The current state of the art for processing GRACE data does not distinguish between these possible ice sheets. We show that the seemingly small uncertainty in the total LGM ice volume (5.01 ± 0.36 mMW equivalent) still allows drastically different ice loads in the central marine Barents Sea. Our analysis confirms the presence of a substantial ice sheet between Svalbard and Franz Josef Land in the north, consistent with some published ice loads (Lambeck, 1996; Auriac *et al.*, 2016). In the southern and central Barents Sea, the RSL and GRACE data are fit equally well by a substantial ice dome (a height of $\sim$2 km of equivalent water load for the 5.37-mMW equivalent case) or next to no ice load at all ($<$500 m for the 4.65-mMW equivalent case). A GRACE observation could be more discriminating if the maximum gravity signal from the LGM could be more precisely located.

A single uplift measurement in the central Barents Sea, even with a modest observational error, would distinguish between the end-member ice configurations, and would be an exciting test of new measurement technologies. Furthermore, we show in *Appendix* S3 that these conclusions do not depend on the mantle rheology chosen. We believe these geometric methods will contribute to our ability to visualize and account for the interplay between ice loads and Earth rheology in models of and predictions from GIA.

Acknowledgements. This project grew out of a larger project funded by Tectonor. Thanks go to Aleksei Amantov, Anna Hormes and especially Willy Fjeldskaar for many helpful conversations and to our anonymous referees for their thorough reading and thoughtful recommendations. We also thank Jan Mangerud for data from the unpublished DATED-2 database. Code for sampling and investigating our ice models can be found at https://github.com/skachuck/barents.

Supporting information

Additional supporting information can be found in the online version of this article.

Table S1. Table of all paleoshoreline emergence records' locations, references and number of observations. Location numbers refer to the locations in Fig. 1.

Figure S1. Time slices (20–13 ka) of the Barents Sea Ice Sheet ice surface heights above solid surface before the modification described in the text. Note the change in scale between the upper and lower rows.

Figure S2. Best-fit model predictions (solid lines) with the most likely 1-sigma prediction range (shaded region) for 368 RSL observations (solid dots) at the 34 locations in Table S1.

Figure S3. The smoothing effect of the lithosphere on two load samples – one with a central dome ($+1\sigma$) and one without (-1σ). The lithosphere elastically supports small-wavelength loads, and so these stresses are not communicated to the mantle for viscoelastic deformation. The effect is that the sharp edges created from our parameterization of the ice sheet are in fact smoothed out, and is effectively replaced with this smoothed model before deformation is computed.

Figure S4. Histogram of RSL residuals (observed minus calculated) for the best-fit ice alteration parameters. (a) All 368 RSL observations, with the best-fit error Gaussian with halfwidth 14 m shown for reference (solid line). (b) Residuals from observations younger than 5 ka and a Gaussian distribution with 2.5-m standard deviation. (c) Residuals for observations between 5 and 10 ka and a 10-m standard deviation.

Figure S5. The sensitivity results of VM2 and parameterizing ICE5G.

Figure S6. The expected reduction of standard deviation for predictions VLGM including (a) a rate of gravity change filtered with a bandpass of 210–600 km and (b) an uplift rate from 73.7°N, 32.5°E in the central Barents Sea, as a function of the error of the observation. Expected uncertainty reductions are shown adding a gravity observation to the RSL data set alone (dotted line) and including a second gravity observation once the GRACE data have already been fit (solid); the vertical line shows the error estimated by Root et al. (2015).

Abbreviations. BSIS, Barents Sea Ice Sheet; GIA, glacial isostatic adjustment; LGM, Last Glacial Maximum.

References

Amantov A, Fjeldskaar W. 2013. Geological-geomorphological features of the Baltic region and adjacent areas: imprint on glacial-postglacial development. *Regional Geology and Metallogeny* **53**: 90–104.

Amantov A, Fjeldskaar W. 2017. Tilted Norwegian postglacial shorelines require a low viscosity asthenosphere and a weak lithosphere. *Journal of Regional Geology and Metallogeny* **70**: 48–59.

Andreassen K, Winsborrow MCM, Bjarnadóttir LR *et al.* 2014. Ice stream retreat dynamics inferred from an assemblage of landforms in the northern Barents Sea. *Quaternary Science Reviews* **92**: 246–257.

Apgar JF, Witmer DK, White FM *et al.* 2010. Sloppy models, parameter uncertainty, and the role of experimental design. *Molecular Biosystems* **6**: 1890–1900.

Auriac A, Whitehouse PL, Bentley MJ *et al.* 2016. Glacial isostatic adjustment associated with the Barents Sea ice sheet: a modelling inter-comparison. *Quaternary Science Reviews* **147**: 122–135.

Bard E, Hamelin B, Fairbanks RG. 1990. U-Th ages obtained by mass spectrometry in corals from Barbados: sea level during the past 130,000 years. *Nature* **346**: 456–458.

Bjarnadóttir LR, Winsborrow MCM, Andreassen K. 2014. Deglaciation of the central Barents Sea. *Quaternary Science Reviews* **92**: 208–226.

Casey FP, Baird D, Feng Q *et al.* 2007. Optimal experimental design in an epidermal growth factor receptor signalling and down-regulation model. *IET Systems Biology* **1**: 190–202.

Cathles L. 1975. *The Viscosity of the Earth's Mantle*. Princeton University Press, Princeton, NJ.

Chachra R, Transtrum MK, Sethna JP. 2011. Comment on 'Sloppy models, parameter uncertainty, and the role of experimental design'. *Molecular Biosystems* **7**, 2522. [author reply: 2523–2524].

Dowdeswell JA, Hogan KA, Evans J *et al.* 2010. Past ice-sheet flow east of Svalbard inferred from streamlined subglacial landforms. *Geology* **38**: 163–166.

Dziewonski AM, Anderson DL. 1981. Preliminary reference Earth model. *Physics of the Earth and Planetary Interiors* **25**: 297–356.

Elverhøi A, Fjeldskaar W, Solheim A *et al.* 1993. The Barents Sea Ice Sheet – A model of its growth and decay during the last ice maximum. *Quaternary Science Reviews* **12**: 863–873.

Fjeldskaar W. 1994. Viscosity and thickness of the asthenosphere detected from the Fennoscandian uplift. *Earth and Planetary Science Letters* **126**: 399–410.

Foreman-Mackey D, Hogg DW, Lang D *et al.* 2013. emcee: the MCMC Hammer. *Publications- Astronomical Society of the Pacific* **125**: 306–312.

Forman SL, Lubinski DJ, Ingólfsson Ó *et al.* 2004. A review of postglacial emergence on Svalbard, Franz Josef Land and Novaya Zemlya, northern Eurasia. *Quaternary Science Reviews* **23**: 1391–1434.

Gjermundsen EF, Briner JP, Akçar N *et al.* 2013. Late Weichselian local ice dome configuration and chronology in Northwestern Svalbard: early thinning, late retreat. *Quaternary Science Reviews* **72**: 112–127.

Grosswald MG. 2001. The Late Weichselian Barents-Kara Ice Sheet: in defense of a maximum reconstruction. *Russian Journal of Earth Sciences* **3**: 427–452.

Hogan KA, Dowdeswell JA, Noormets R *et al.* 2010. Evidence for full-glacial flow and retreat of the Late Weichselian Ice Sheet from the waters around Kong Karls Land, eastern Svalbard. *Quaternary Science Reviews* **29**: 3563–3582.

Honsho C, Kido M. 2017. Comprehensive analysis of traveltime data collected through GPS-acoustic observation of seafloor crustal movements. *Journal of Geophysical Research: Solid Earth* **122**: 8583–8599.

Hormes A, Akçar N, Kubik PW. 2011. Cosmogenic radionuclide dating indicates ice-sheet configuration during MIS 2 on Nordaustlandet, Svalbard. *Boreas* **40**: 636–649.

Hormes A, Gjermundsen EF, Rasmussen TL. 2013. From mountain top to the deep sea – deglaciation in 4D of the northwestern Barents Sea ice sheet. *Quaternary Science Reviews* **75**: 78–99.

Hughes ALC, Gyllencreutz R, Lohne ØS *et al.* 2016. The last Eurasian ice sheets – a chronological database and time-slice reconstruction, DATED-1. *Boreas* **45**: 1–45.

Ingólfsson Ó, Landvik JY. 2013. The Svalbard-Barents Sea ice-sheet – historical, current and future perspectives. *Quaternary Science Reviews* **64**: 33–60.

Jakobsson M, Mayer L, Coakley B *et al.* 2012. The International Bathymetric Chart of the Arctic Ocean (IBCAO) version 3.0. *Geophysical Research Letters* **39**: 1–6.

Jessen SP, Rasmussen TL, Nielsen T *et al.* 2010. A new Late Weichselian and Holocene marine chronology for the western Svalbard slope 30,000–0 cal years BP. *Quaternary Science Reviews* **29**: 1301–1312.

Kachuck SB. 2017 *giapy: Glacial Isostatic Adjustment in PYthon.* [source code] https://github.com/skachuck/giapy.

Kendall RA, Mitrovica JX, Milne GA. 2005. On post-glacial sea level – II. Numerical formulation and comparative results on spherically symmetric models. *Geophysical Journal International* **161**: 679–706.

Lambeck K. 1995. Constraints on the Late Weichselian ice sheet over the Barents Sea from observations of raised shorelines. *Quaternary Science Reviews* **14**: 1–16.

Lambeck K. 1996. Limits on the areal extent of the Barents Sea ice sheet in Late Weichselian time. *Global and Planetary Change* **12**: 41–51.

Landvik JY, Bondevik S, Elverhøi A *et al.* 1998. The Last Glacial Maximum of Svalbard and the Barents Sea area: ice sheet extent and configuration. *Quaternary Science Reviews* **17**: 43–75.

Mannakee BK, Ragsdale AP, Transtrum MK, *et al.* 2016. Sloppiness and the geometry of parameter space. In *Uncertainty in Biology*, Vol. **17**, Geris L, Gomez-Cabrero D (eds), Springer International Publishing, Switzerland; 471.

Milne GA, Mitrovica JX. 1998. Postglacial sea-level change on a rotating Earth. *Geophysical Journal International* **133**: 1–19.

Mitrovica JX, Forte AM, Simons M. 2000. A reappraisal of postglacial decay times from Richmond Gulf and James Bay, Canada. *Geophysical Journal International* **142**: 783–800.

Nield GA, Barletta VR, Bordoni A *et al.* 2014. Rapid bedrock uplift in the Antarctic Peninsula explained by viscoelastic response to recent ice unloading. *Earth and Planetary Science Letters* **397**: 32–41.

Ottesen D, Dowdeswell JA, Landvik JY *et al.* 2007. Dynamics of the Late Weichselian ice sheet on Svalbard inferred from high-resolution sea-floor morphology. *Boreas* **36**: 286–306.

Pavlidis YA, Dunaev NN, Shcherbakov FA. 1990. *Actual Problems of the Barents Sea Quaternary Geology.* [*Sovremenye Protsessy Osadkona-Kopleniya Na Shel'fe Mirovogo Okeana*]. Nauka: Moscow; 76–93 [in Russian].

Pavlidis YA, Murdmaa I, Ivanova E *et al.* 2001. Were Novaya Zemlya and Franz Josef Land ice sheets connected 18 kyr BP? In *Experience of Systemic Oceanological Investigations in the Arctic*, Lisitzin AP, Vinogradov ME, Romankevich EA (eds). Scientific Publishing: Moscow; 456–467 [in Russian].

Peltier WR. 2004. Global Glacial isostasy and the surface of the Ice-Age Earth: the ICE-5G (VM2) model and GRACE. *Annual Review of Earth and Planetary Sciences* **32**: 111–149.

Peltier WR, Argus DF, Drummond R. 2015. Space geodesy constrains ice age terminal deglaciation: the global ICE-6G_C (VM5a) model. *Journal of Geophysical Research: Solid Earth* **120**: 450–487.

Root BC, Tarasov L, Van Der Wal W. 2015. GRACE gravity observations constrain Weichselian ice thickness in the Barents Sea. *Geophysical Research Letters* **42**: 3313–3320.

Rüther DC, Mattingsdal R, Andreassen K *et al.* 2011. Seismic architecture and sedimentology of a major grounding zone system deposited by the Bjørnøyrenna Ice Stream during Late Weichselian deglaciation. *Quaternary Science Reviews* **30**: 2776–2792.

Siegert MJ, Dowdeswell JA. 1995. Numerical modeling of the Late Weichselian Svalbard-Barents Sea ice sheet. *Quaternary Research* **43**: 1–13.

Simon KM, James TS, Henton JA *et al.* 2016. A glacial isostatic adjustment model for the central and northern Laurentide Ice Sheet based on relative sea level and GPS measurements. *Geophysical Journal International* **205**: 1618–1636.

Solheim A, Russwurm L, Elverhøi A *et al.* 1990. Glacial geomorphic features in the northern Barents Sea: direct evidence for grounded ice and implications for the pattern of deglaciation and late glacial sedimentation. *Geological Society, London, Special Publications* **53**: 253–268.

Stokes CR, Tarasov L, Blomdin R *et al.* 2015. On the reconstruction of palaeo-ice sheets: recent advances and future challenges. *Quaternary Science Reviews* **125**: 15–49.

Waterfall JJ, Casey FP, Gutenkunst RN *et al.* 2006. Sloppy-model universality class and the Vandermonde matrix. *Physical Review Letters* **97**: 150601.

Winsborrow MCM, Andreassen K, Corner GD *et al.* 2010. Deglaciation of a marine-based ice sheet: Late Weichselian palaeo-ice dynamics and retreat in the southern Barents Sea reconstructed from onshore and offshore glacial geomorphology. *Quaternary Science Reviews* **29**: 424–442.